Universiteit Leiden
The Netherlands

Radio-loud AGN morphology and host-galaxy properties in the LOFAR Two-metre Sky Survey Data Release 2

Clews, L.; Croston, J.H.; Dickinson, H.; Mingo, B.; Hardcastle, M.J.; Barkus, B.; ... ; Röttgering, H.J.A.

Citation
Clews, L., Croston, J. H., Dickinson, H., Mingo, B., Hardcastle, M. J., Barkus, B., ... Röttgering, H. J. A. (2026). Radio-loud AGN morphology and host-galaxy properties in the LOFAR Two-metre Sky Survey Data Release 2. *Monthly Notices Of The Royal Astronomical Society, 541*(4), 3452-3467. doi:10.1093/mnras/staf966

Version:	Publisher's Version
License:	Creative Commons CC BY 4.0 license
Downloaded from:	https://hdl.handle.net/1887/4292959

Note: To cite this publication please use the final published version (if applicable).

Monthly Notices of the ROYAL ASTRONOMICAL SOCIETY

MNRAS **541,** 3452–3467 (2025) https://doi.org/10.1093/mnras/staf966
Advance Access publication 2025 June 12

Radio-loud AGN morphology and host-galaxy properties in the LOFAR Two-metre Sky Survey Data Release 2

L. Clews,[1]★ J. H. Croston,[1] H. Dickinson,[1] B. Mingo,[2] M. J. Hardcastle,[2] B. Barkus,[2] J. M. G. H. J. de Jong[3] and H. J. A. Röttgering[3]

[1]*School of Physical Sciences, Open University, Walton Hall, Milton Keynes MK7 6AA, UK*
[2]*Centre for Astrophysics Research, University of Hertfordshire, College Lane, Hatfield AL10 9AB, UK*
[3]*Leiden Observatory, Leiden University, PO Box 9513, NL-2300 RA Leiden, the Netherlands*

Accepted 2025 June 6. Received 2025 May 12; in original form 2025 February 17

ABSTRACT

Radio-loud active galaxies (RLAGN) can exhibit various morphologies. The Fanaroff–Riley (FR) classifications, which are defined by the locations of peaks in surface brightness, have been applied to many catalogues of RLAGN. The FR classifications were initially found to correlate with radio luminosity. However, recent surveys have demonstrated that radio luminosity alone does not reliably predict radio morphology. We have devised a new semi-automated method involving ridgeline characterizations to compile the largest known classified catalogue of RLAGN to date, with data from the LOFAR (LOw Frequency ARray) Two-metre Sky Survey Data Release 2. We reassess the FR divide and its cause by examining the physical and host galaxy properties of 3590 FRIIs (FR type II) and 2354 FRIs (FR type I) (at $z \leq 0.8$). We find that RLAGN near the FR divide with $10^{25} \leq L_{144} \leq 10^{26}$ WHz^{-1} are more likely to show FRI over FRII morphology if they occupy more massive host galaxies. We find no correlation, when considering selection effects, between the FR break luminosity and stellar mass or host-galaxy rest-frame absolute magnitude. Overall, we find the cause of the different radio morphologies in this sample to be complex. Considering sources near the FR divide with $10^{25} \leq L_{144} \leq 10^{26}$ WHz^{-1}, we find evidence to support the inner environment having a role in determining jet disruption. We make available a public catalogue of morphologies for our sample, which will be of use for future investigations of RLAGN and their impact on their surroundings.

Key words: galaxies: active – galaxies: jets – radio continuum: galaxies.

1 INTRODUCTION

Active galactic nuclei (AGN) are compact regions at the centre of some galaxies that emit radiation across the electromagnetic spectrum. AGN that have large regions of radio emission (also known as radio lobes) that can extend well beyond the visible structure of the host galaxy are known as radio-loud AGN (RLAGN) or radio galaxies. These regions are driven by collimated outflows of plasma from the AGN, known as radio jets, at relativistic speeds on parsec (pc) to Mpc scales (see e.g. Begelman, Blandford & Rees 1984; Bridle & Perley 1984; Hardcastle & Croston 2020, for an in-depth review).

Extended RLAGN can exhibit various morphologies (e.g. Miley 1980), but will most commonly consist of one of two categories established by Fanaroff & Riley (1974): Fanaroff–Riley (FR) type I (FRI) or FR type II (FRII). FRI sources are defined to be centre-brightened, whilst FRII sources are edge-brightened. The FR classifications are widely used and have been applied to numerous surveys. With these classifications, Fanaroff & Riley (1974) suggested a correlation between the relative positions of high and low radio surface brightness (SB; flux density per unit area) regions of RLAGN and radio luminosity in the 3CR sample (Mackay 1971).

The physical cause of the FR divide remains under debate. For example, it has been suggested that accretion mode could influence jet morphology. A direct link between the two would mean that the properties of the launched jet are determined by the AGN accretion disc or flow, such that jets are intrinsically different when they are launched. This is also known as the central engine model (Jackson & Rawlings 1997; Meyer et al. 2011; Keenan et al. 2021). However, this model cannot explain why jets of the same inferred power are able to turn into different morphologies (Hardcastle & Croston 2020; Mingo et al. 2022). FRIIs are thought to remain relativistic for the full length of their jets until terminating in a hotspot, while FRIs are known to be initially relativistic and then become mass loaded due to entrainment, causing them to decelerate on kpc scales (Bicknell 1994; Laing & Bridle 2002; Wykes et al. 2015; Tchekhovskoy & Bromberg 2016; Hardcastle & Croston 2020). Properties of the central engine alone cannot account for this structural difference. Instead, observations of kpc-scale jet deceleration suggest a relationship between jet power and host-scale environmental density such that jets of the same initial power will remain collimated and relativistic in a poor environment and decelerate, entrain material, and expand in a richer one.

★ E-mail: lucy.clews@open.ac.uk

© The Author(s) 2025.
Published by Oxford University Press on behalf of Royal Astronomical Society. This is an Open Access article distributed under the terms of the Creative Commons Attribution License (https://creativecommons.org/licenses/by/4.0/), which permits unrestricted reuse, distribution, and reproduction in any medium, provided the original work is properly cited.

Downloaded from https://academic.oup.com/mnras/article/541/4/3452/8161029 by Bibliotheek Instituut Moleculaire Plantkunde user on 30 January 2026

There is some observational evidence to support this theory. Ledlow & Owen (1996) found the FRI/FRII luminosity break to be dependent on host-galaxy magnitude, such that FRIs have higher radio luminosities when in brighter host galaxies [where the density of the interstellar medium (ISM) is assumed to be higher]. However, this result has since been questioned due to severe selection effects in the sample (Best 2009; Lin et al. 2010; Capetti, Massaro & Baldi 2017; Hardcastle & Croston 2020), so it is not known whether it holds for the full population of RLAGN. In addition, interpreting the results of Ledlow & Owen (1996) in the context of a jet disruption model relies on radio luminosity being a good proxy for jet power. Differences in particle content, external pressure, and radiative losses mean that this conversion is known to have large systematic biases and scatter (for more details see section 4.5 of Hardcastle & Croston 2020 or Croston, Ineson & Hardcastle 2018; Hardcastle 2018).

The result also uses host-galaxy absolute magnitude as an estimator for the density of material available to disrupt jets. Mass loading in FRIs can occur by different methods. The primary mechanism considered in the literature is external entrainment from hot gas in the surrounding ISM (Bicknell 1994; Laing & Bridle 2002). For massive elliptical galaxies, which are the typical hosts of RLAGN, the host-galaxy environmental richness is expected to scale with galaxy mass (Best et al. 2005; Kim & Fabbiano 2013), for which absolute magnitude is a proxy (Kondapally et al. 2022). An alternative mechanism is internal entrainment, where mass is loaded from stellar winds from stars embedded within the jet. In this scenario, the density of young stellar populations could be more important than the host galaxy stellar mass. Mass loading from stellar winds has been argued to be sufficient to decelerate FRI–jets in some cases (Komissarov 1994; Bowman, Leahy & Komissarov 1996; Hubbard & Blackman 2006; Wykes et al. 2015). However, Perucho et al. (2014) found for FRIs of typical power ($L_j \approx 10^{43}$–10^{44} erg s^{-1}), stellar winds alone do not produce significant deceleration.

In more recent years, as radio surveys have improved to reach lower flux limits, evidence has emerged that morphology is not as closely related to luminosity as originally believed. An unexpected population of low-luminosity FRIIs (FRII-lows) was recently discovered (Best 2009; Capetti et al. 2017; Mingo et al. 2019, 2022), which form a substantial proportion of FRIIs below $z \sim 0.8$ (Mingo et al. 2019, 2022). It is now known that there is a large overlap in the luminosity distributions of FRIs and FRIIs (Gendre, Best & Wall 2010; Mingo et al. 2019, 2022; de Jong et al. 2024a), complicating the interpretation of the two different morphologies and how they are caused. Currently, evidence points to FRII-lows being a mix of RLAGN populations (Mingo et al. 2019, 2022). One theory is that FRII-lows could occupy lower mass hosts, so they can remain collimated even though they have a relatively low power (Mingo et al. 2019). Another possibility is that FRII-lows are no longer active, just fading. In this case, they would not be comparable to active sources. Comparisons have been made between FRII-lows and FRIs of similar luminosities and physical size. The probability of a jet of intermediate luminosity becoming an FRI or FRII was shown to depend on the stellar mass of the host galaxy (Mingo et al. 2022). A relationship between jet power and host-galaxy magnitude has not yet been ruled out; Mingo et al. (2019) showed some evidence to support the Ledlow–Owen relation, but could not rule out that the observed relation was due to selection effects.

Host-galaxy scale environmental interactions with the jet can impact source morphology. For some low-power sources, large-scale environmental interactions can cause the outer portion of the jet to bend or distort away from a linear trajectory. The FRIs of this subclass are known as bent-tailed (BT) sources (O'Brien et al. 2018; Mingo et al. 2019), which can be subclassified based on their opening angle, $\theta_{\rm open}$. BTs with $\theta_{\rm open} > 90^\circ$ are known as wide-angle tailed (WAT) sources (Owen & Rudnick 1976a; Mingo et al. 2019), whilst BTs with $\theta_{\rm open} < 90^\circ$ are narrow-angle tailed (NAT; Rudnick & Owen 1976; O'Dea & Owen 1985; Mingo et al. 2019). The favoured explanation for BTs is that they form in dense environments such as galaxy clusters (Owen & Rudnick 1976b; Blanton 2000; Blanton et al. 2001; Wing & Blanton 2011; Morris et al. 2022; De Gazon et al. 2023), where they are bent by ram pressure (Jones & Owen 1979; Burns & Owen 1980; Blanton 2000; Morsony et al. 2013). As a result, BTs have been used to identify galaxy clusters at high redshift (Wing & Blanton 2011; Blanton 2015; Golden-Marx et al. 2021). However, BTs have also been found in galaxy groups (Ekers 1978; Freeland & Wilcots 2011), in filaments (Edwards, Fadda & Frayer 2010), and in isolated environments where the intracluster medium is not likely to be dense enough to generate ram pressure (Blanton et al. 2001).

The relationship between morphology and environment is clearly vital to understanding the FR break and the diversity of the RLAGN population. The LOFAR (LOw Frequency ARray) Two-metre Sky Survey (LoTSS) provides a unique opportunity to explore the RLAGN population using the largest sample to date, with unmatched sensitivity to extended structure on 6 arcsec scales. Our motivation for this work is to derive an automated classification technique suited to large samples, which produces groups of sources with similar jet morphologies and low contamination, motivated by the physical properties of each source. A large morphologically classified catalogue has the potential to greatly improve our understanding of how radio sources evolve and affect their environment under different conditions at different redshifts. This could then be applied to exploring the locations and mechanisms of AGN feedback. As such, we want to explore all of the information available rather than applying a standardised set of rules that would produce binary classifications. The aim is to produce clean classifications of objects, rather than to obtain complete population statistics or classify every single source.

This paper is structured as follows. In Section 2, we describe the details of our dataset derived from LoTSS Data Release 2 (DR2; Shimwell et al. 2022). In Section 3, we outline our classification method, and then present the morphological and environmental properties of our sample in Section 4. In Section 5, we discuss our interpretation of the results for the different populations before presenting conclusions in Section 6.

2 DATA

This section outlines how we derived a sample of RLAGN suitable for automated classification. Section 2.1 describes our starting catalogue. Section 2.2 explains our decision to use ridgelines (Barkus et al. 2022) for this method and the selection criteria applied to them. We then explain how we use ridgelines to extract structural and morphological information about the sources in our sample in Sections 2.3 and 2.4.

2.1 AGN sample selection

The data sets used in this work are from the LoTSS DR2 (Shimwell et al. 2022). LoTSS is an ongoing survey of the Northern Sky at 120–168 MHz with 6 arcsec resolution. LoTSS DR2 contains over four million sources across 27 per cent of the Northern Sky. Of these, 85 per cent have optical host galaxy identifications and 58 per cent have good spectroscopic or photometric redshifts (Williams et al.

Downloaded from https://academic.oup.com/mnras/article/541/4/3452/8161029 by Bibliotheek Instituut Moleculaire Plantkunde user on 30 January 2026

2019; Hardcastle et al. 2023). For further details and validation of the quality of host-galaxy identifications, see Hardcastle et al. (2023).

We make use of the 6 arcsec Stokes *I* images, which have a central frequency of 144 MHz and median rms sensitivity of 83 μJy beam^{-1}. The calibration process of the LoTSS fields is described by Shimwell et al. (2022) and treats both direction-dependent and direction-independent effects (Tasse et al. 2021). We restrict our sample to the LoTSS DR2 AGN catalogue (Hardcastle et al. 2025, hereafter H25), which contains 666 804 sources. This catalogue was designed to select a clean sample of radio-loud AGN.

2.2 Ridgeline data

Ridgelines trace the pathway of highest radio flux density along a jet (e.g. Barkus et al. 2022). Each point along the ridgeline is calculated as the maximum flux along an annular slice at a distance set by the user (in this case, the beam size of LOFAR), within the set search sector (of half-size 60°). The maximum ridgeline length is set to 0.95 × source size from the initial point, in both search directions. Preliminary work by Barkus et al. (2022) indicated the usefulness of ridgelines for morphological characterisation – they record SB information and provide a unique measure of jet size as the distance over which material has travelled along the jet path. Ridgelines are expected to pass through the centre of the optical/infrared host galaxy of a radio source and have been applied as part of the host galaxy identification process for LoTSS DR2 (Hardcastle et al. 2023).

The ridgeline code, RL-XID,[1] has been applied to a subset of extended sources in LoTSS DR2 (>15 arcsec and >10 mJy), for which they were expected to provide useful morphological information (described by H25).In this work, we use ridgelines to find clean samples of RLAGN with similar jet morphologies. Our initial sample consists of all sources in H25 that have a ridgeline (56 161). These sources have between 3 and 35 points along their ridgeline, but most (94.4 per cent) have fewer than 20. Due to our method uniquely relying on ridgelines, it was vital that we apply some initial ridgeline quality filters. We chose to limit our sample to sources in H25 with >5 ridgeline points, to ensure each source was sufficiently well sampled for our analysis. After this filter, there were 50 234 sources remaining. We discuss the effect of angular size-related cuts on our sample selection and results in Section 3.5.

2.3 Ridgeline analysis

We fit a spline model with natural boundary conditions to each ridgeline in our sample to smooth them as well as to obtain a differentiable function that describes the ridgeline. Due to the complex nature of RLAGN, the ridgelines that trace them can have bends of varying size and degree. It can be impossible to set up a Cartesian coordinate system where all points on the ridgeline have unique values of both the x and y coordinates. Instead, the ridgelines are best characterised by a parametric spline. We defined a third-order, uniform parametrization with 200 linearly spaced points corresponding to linearly spaced values of the spline parameter. We chose to use 200 spline points as this is much greater than the number of points on any ridgeline (which will have maximum ∼30 points) by a large enough margin that the spline would be interpolating across a very small distance with each iteration, resulting in a smooth representation of the ridgeline. The spline had to be differentiable to at least second order for later analysis (see Section 2.4), so a polynomial of minimum order 3 was required. We experimented with higher orders and found they did not produce smoother representations of the ridgelines.

We also fitted an interpolating cubic spline to the SB profiles generated by RL-XID for each source in our sample of equal length to the parametric ridgeline splines. The SB of an individual pixel in RL-XID is defined as the weighted average of the centre pixel and the 4 orthogonally adjacent pixels. To exclude sources with low signal-to-noise ratio that would be difficult to classify, we limited our sample to sources with a peak to mean SB ratio (dynamic range) greater than 2, leaving 49 799 sources with SB information. These SB spline profiles were used in the first stage of our classification method, described in Section 3.

2.4 Curvature analysis

As an additional means of classification, we chose to quantify the curvature (κ) of the ridgelines to explore the properties of BTs. The curvature of a line can be measured over short increments (or arclengths, s) along it as a function, $f(x)$, of ψ, the angle which a tangent to the ridgeline at that point makes with the positive x-axis. The definition of κ used in this paper is

$$\kappa = \frac{\mathrm{d}\psi}{\mathrm{d}s} = \frac{\mathrm{d}\psi}{\mathrm{d}x} \Big/ \frac{\mathrm{d}s}{\mathrm{d}x} = \frac{f''(x)}{(1 + f'(x)^2)^{3/2}}, \tag{1}$$

where

$$\frac{\mathrm{d}\psi}{\mathrm{d}x} = \frac{f''(x)}{(1 + f'(x)^2)}, \quad \frac{\mathrm{d}s}{\mathrm{d}x} = (1 + f'(x)^2)^{1/2}.$$

In our case, the function describing the ridgeline is unknown. Instead, we have a differentiable parametric spline model (of order $k = 3$ and 200 points) for each ridgeline. We use the parametric curvature equation given by

$$\kappa = \frac{\dot{x}\ddot{y} - \dot{y}\ddot{x}}{(\dot{x}^2 + \dot{y}^2)^{3/2}}, \tag{2}$$

where u is a uniform parameter, $\dot{x} = \mathrm{d}x/\mathrm{d}u$, $\dot{y} = \mathrm{d}y/\mathrm{d}u$, $\ddot{x} = \mathrm{d}^2x/\mathrm{d}u^2$, and $\ddot{y} = \mathrm{d}^2y/\mathrm{d}u^2$.

For every source in our sample, we obtain a curvature profile. Fig. 1 shows an example of the structural information (ridgeline spline, SB spline profile, and curvature) extracted from the ridgelines for each source in our sample. Both the magnitude and direction of curvature along the jet path are useful quantities to classify the morphology of RLAGN. We incorporate curvature as a secondary step in our classification process (described in Section 3).

3 CLASSIFICATION METHOD

The aim of this work is to identify clean samples of objects with similar jet morphologies, whilst accounting for their physical properties, in an automated way. This section outlines our classification method, which uses the ridgeline structure information described in the previous section. In Section 3.1, we describe how we reduced the dimensionality of our SB spline profiles before using unsupervised density-based clustering to place them into groups with similar features. Next, we explain how host galaxy locations were incorporated into classifying morphology in Section 3.2 (with more detail in Appendix A). We then outline our method for calculating the jet opening angle on a subset of sources and its usefulness in identifying BTs in Section 3.3. We then explain how final morphological classifications were assigned using a combination of SB, host location, curvature, and opening angles in Section 3.4. Lastly, in Section 3.5, we consider selection effects.

[1] https://github.com/BonnyBlu/RL-Xid

Downloaded from https://academic.oup.com/mnras/article/541/4/3452/8161029 by Bibliotheek Instituut Moleculaire Plantkunde user on 30 January 2026

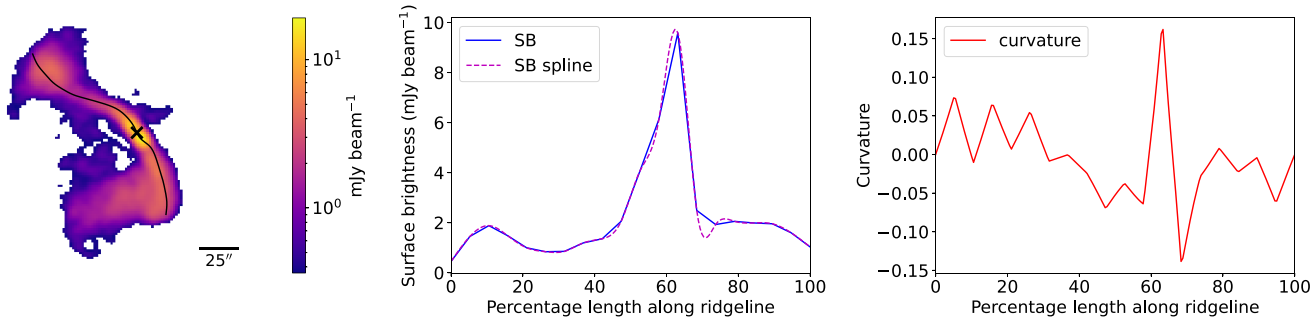

Figure 1. Example of input data. Left: LoTSS DR2 source ILT J090543.94+422105.9 and its ridgeline spline. The closest ridgeline spline point to the host galaxy position is indicated by a cross. Middle: SB profile obtained from RL-XID overlaid with its spline model. Right: Curvature profile.

Table 1. Overview of the UMAP and HDBSCAN parameters used.

UMAP parameters		HDBSCAN parameters	
Parameters	Number	Parameter	Number
Number of neighbours	400	Minimum sample	100
Minimum distance	1×10^{-3}	Minimum cluster size	800
Number of components	2	Maximum cluster size	8500
Repulsion strength	24		

3.1 Dimensionality reduction and clustering

We first used the Uniform Manifold Approximation and Projection (UMAP) algorithm (McInnes, Healy & Melville 2018) to embed our 200-dimensional SB spline data into two dimensions in a way that best preserves the overall structure of the higher dimensional data. We used the UMAP-LEARN[2] implementation of the UMAP algorithm using the parameters listed in Table 1.

The next step in our method was to separate the RLAGN in our sample into clusters with similar features in their SB spline profiles, without feeding in any preconceptions of known classes. Due to the nature of this approach, the number of clusters expected was not known. We chose to use the Hierarchical Density-Based Spatial Clustering of Applications with Noise (HDBSCAN) algorithm (Campello 2013; McInnes, Healy & Astels 2017) as it does not require prior knowledge of how many clusters are expected and allows for groups of varying size and densities, unlike some other density-based clustering algorithms.

This technique has not been used to group LOFAR RLAGN before. Other automated methods have inputted LOFAR images directly into neural networks (e.g. Lukic et al. 2019; Mostert et al. 2021; Baron Perez et al. 2025). This method uses ridgelines to parametrize the images before using them for classification. The advantage of this method is that it should separate sources into groups with similar jet morphologies, which can then be used to study jet evolution under different conditions.

We ran HDBSCAN on our previously defined UMAP embedding using the parameters in Table 1. We experimented with the HDBSCAN parameters until we found values that produced clusters that contained sufficiently similar SB profile characteristics, i.e. numbers and locations of SB peaks, overall shape, and whether 'nearby' clusters appeared sufficiently distinct. With these parameters, HDBSCAN clustered 82.1 per cent of our sample (40 903 sources) into 25 clusters of varying size; the remaining sources were classified by HDBSCAN as 'noise'. Fig. 2 shows two example SB cluster groups and images of three randomly selected sources from within them. We visually inspected 100 sources from each cluster group to check if they were morphologically similar. We estimated that typically 70 per cent of sources in each cluster group were morphologically similar before host galaxy locations were considered. We also found that some of the HDBSCAN groups had very similar morphological characteristics to each other, e.g. with reflected locations of peak brightness. To reduce the amount of contamination, we calculated the mean SB spline profile for each cluster group and reassigned sources with five or more SB spline points that were 3 or more standard deviations away from the mean profile of their original cluster to the cluster group they fit best. The new best-fitting group was determined by the smallest value of the mean squared error between the outlying profile and the mean spline profile of each SB cluster. We chose this threshold of spline points and number of standard deviations after experimenting with different values, each time checking that the remaining profiles had similar shapes and obvious large outliers were identified.

After this reassignment, we again visually inspected a random sample of 100 sources from each SB cluster. We found that the remaining contamination within the HDBSCAN cluster groups was from sources of smaller angular size or sources with an unusual host galaxy location. As the aim of this work is to produce clean classes of sources, we applied an additional filter to restrict our final sample to sources with the largest angular size (LAS) > 45 arcsec. We discuss the potential implications of this on our scientific conclusions and future work in Section 3.5.

3.2 Host subgroups

There may be classes of objects that have similar SB profiles but have host galaxies that are located at substantially different locations along them. The location of the host galaxy provides important information on the formation history and symmetry of the jets (the distance of each jet from the host galaxy). Sources with a host in the centre are a different class of objects from those with a host towards the end of the ridgeline. It is also possible that sources with hosts at uncommon locations compared to their SB class have incorrect host IDs. The next step in our classification pipeline was to incorporate the location of host galaxies to distinguish between situations with differing jet physics and to identify outliers with incorrect IDs.

We first calculated the closest point along the ridge spline to the host galaxy position and expressed this as a relative length along the ridgeline spline, to make host galaxy positions comparable among RLAGN with very different projected sizes on the sky. We then visually inspected the distribution of host galaxy locations along the ridgelines for each SB cluster identified by HDBSCAN. A very

[2]https://github.com/lmcinnes/umap

Downloaded from https://academic.oup.com/mnras/article/541/4/3452/8161029 by Bibliotheek Instituut Moleculaire Plantkunde user on 30 January 2026

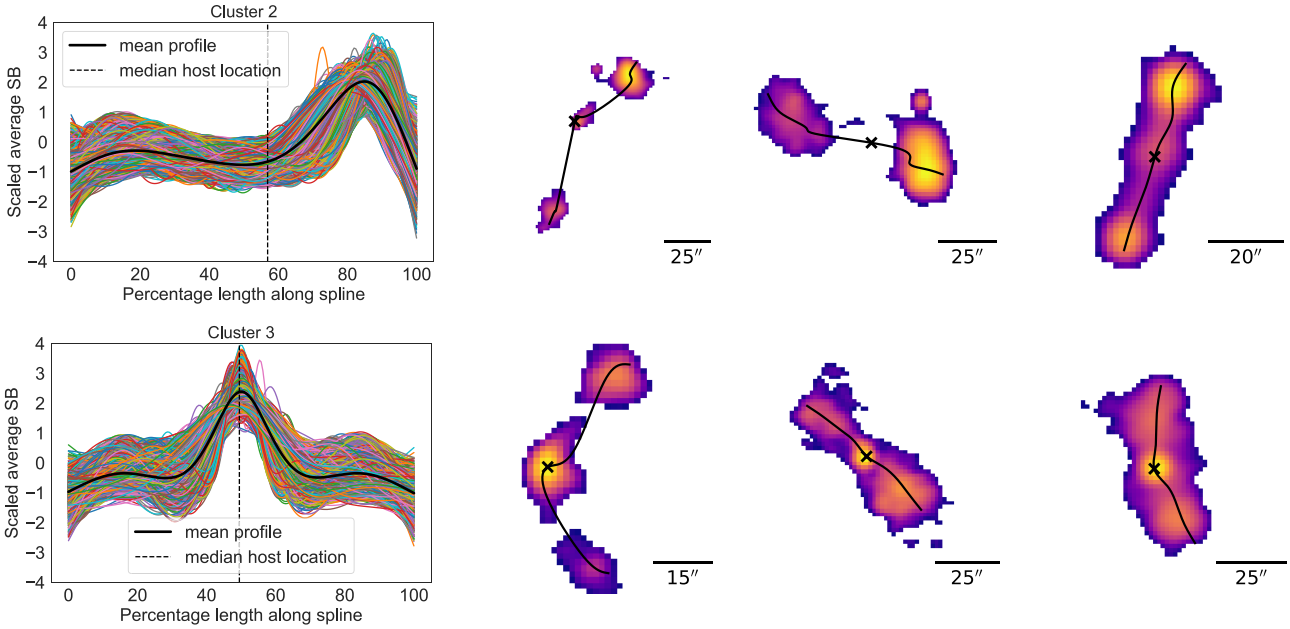

Figure 2. Left: Two example SB clusters generated by HDBSCAN, corresponding to FRII-like (top) and FRI-like (bottom) sources. Each SB profile is scaled by z-score standardization and represented by a different coloured line. The bold, solid line on each figure represents the mean SB profile of that cluster. The vertical dashed line represents the median host galaxy location of the cluster. Right: Three randomly chosen example sources from the SB clusters, overlaid with their ridgeline spline. The cross indicates the location of the closest ridgeline spline point to the host galaxy position.

small proportion of sources (3 per cent of the total amount clustered) had host galaxies positioned within the first or last 10 per cent of their ridgeline splines. We visually inspected all of these sources and found the majority to have incomplete ridgelines or incorrect host IDs. We, therefore, decided to remove this small proportion of sources from our sample. We do not believe that this decision will discard BT sources that have been correctly traced by the ridgelines and, therefore, could have been used for our analysis. The ridgelines are designed to stop tracing when they either find no additional points above a brightness threshold of four times the locally measured rms or reach the maximum ridgeline length (defined by Barkus et al. 2022). In addition, we did not find correctly traced BTs in this group when performing the visual inspection.

We also found that for each cluster, there were between one and three peaks in the distributions of host galaxy locations. We used Gaussian mixture modelling (GMM) to separate these (see Appendix A). Sources with host galaxy locations that were within 1σ, 2σ, and 3σ of their Gaussian group mean were assigned quality flags of Q1, Q2, and Q3, respectively. Sources whose host location was more than 3σ deviant were excluded. In total, we had 20 172 sources placed into host subgroups with a quality flag of Q1–3. We consider Q1 sources as 'good quality' and only use these for scientific analysis in Section 4. Q2 and Q3 sources are not used in our analysis due to having atypical host locations in comparison to the rest of their SB cluster, which could indicate that they have different jet dynamics. Nevertheless, we consider the impact of including Q2 sources on our conclusions in Section 4.

We again visually inspected a random sample of 100 source images from each subgroup. Of each Q1 subgroup we typically found >90 per cent of sources to be morphologically similar. Of the sources that were not, most often the ridgeline did not represent the source accurately or appeared to have an incorrect host ID. We found that subgroups of Q3 were of lower purity, typically with 70 per cent or less of sources being morphologically similar. We explain how we use the host subgroups for classification in Section 3.4.

3.3 Opening angles

We noticed some BT sources within the FRI SB clusters when performing our visual inspections. This is to be expected because they have FRI-like gradually decreasing SB profiles. BT sources are traditionally defined by their opening angle, $\theta_{\rm open}$. We used the ridgelines to explore $\theta_{\rm open}$ of the FRI SB clusters, to identify the BTs within them. We limited the sample for which $\theta_{\rm open}$ was to be calculated to the largest (eight or more ridgeline points) and most intrinsically curved sources (maximum absolute curvature amplitude $|\kappa_{\rm max}| > 0.2$, see Section 2.4) in the FRI subgroups found by our clustering method.

The tails of BT sources are bent in the same direction. To filter for this, we used curvature information. Where the ridgeline splines were curved in the same direction (had opposite curvature magnitudes) at the first and last 10 per cent, $\theta_{\rm open}$ was calculated by taking the dot product between two vectors $\boldsymbol{HA}$ and $\boldsymbol{HB}$:

$$\theta_{\rm open} = \cos^{-1}\left(\frac{\boldsymbol{HA}\cdot\boldsymbol{HB}}{|\boldsymbol{HA}||\boldsymbol{HB}|}\right). \quad (3)$$

$\boldsymbol{HA}$ was initially calculated between the host galaxy (H) and the ridgeline spline point (A) immediately prior to H. $\boldsymbol{HB}$ was initially taken between H and the ridgeline spline point (B) immediately after H. The ridgeline spline points are spaced equally. With each iteration, B and A were shifted by one step in the forward and backward direction along the ridgeline, respectively. $\theta_{\rm open}$ was calculated during each iteration, until one end of the ridgeline was reached. We obtained an opening angle profile for each BT source candidate, beginning at the host galaxy, moving out towards the ends of the source. If the opening angle profile was found to decrease, the source was classified as 'bent'. An example opening angle profile is shown in Fig. 3.

Downloaded from https://academic.oup.com/mnras/article/541/4/3452/8161029 by Bibliotheek Instituut Moleculaire Plantkunde user on 30 January 2026

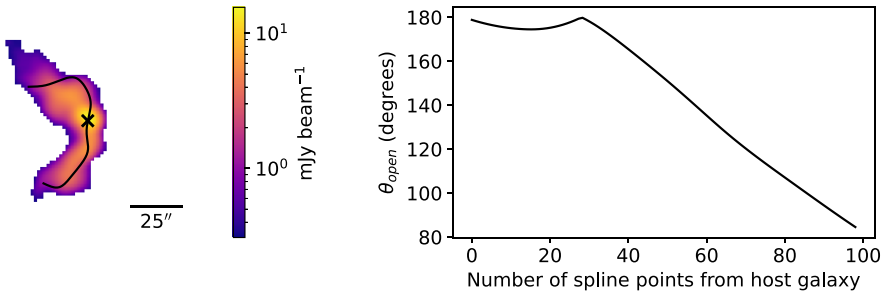

Figure 3. Left: Example 'bent' source with ridgeline spline and closest ridgeline spline point to the host galaxy (indicated by a cross) shown. Right: Opening angle profile as a function of point number away from the host galaxy.

We visually inspected all of the 'bent' sources, as there were only 223 of them. We found all of them to have bent ridgelines, but estimate only 75 per cent of them to be bent sources. Where the source was not bent, the ridgeline did not follow the lobe or tail structure of the jet in the best way. The focus in Barkus et al. (2022) was on the validity of the ridgelines for host identification, so they are not optimised for all classes of source. We describe how we use this information in the final stage of our classification method and planned future work in Section 3.4.

3.4 Classification

At this stage in our method, we had identified SB clusters using HDBSCAN, subgrouped these based on host galaxy positions, and used ridgeline opening angles to identify 'bent' sources within the FRI-like subgroups. This section describes how we combined all of the available information and assigned labels to sources. A flowchart of this process is shown in Fig. 4 and final descriptions of classes are outlined in Table 2.

Edge-brightened subgroups where the host galaxy position was within the central Gaussian of its host distribution were labelled as 'FRIIs', consisting of 5410 sources. Of these FRIIs, 3590 are labelled as Q1 FRIIs. These are sources where we can be most confident of the host ID. Edge-brightened subgroups where the host galaxy was not in the central Gaussian distribution were classified as 'uncertain FRIIs'. This class has 1288 sources.

We took all of the subgroups of centre-brightened morphology with host galaxies located in the central Gaussian of their distribution and combined them as having FRI-like morphology. We then used the method described in Section 3.3 to identify 223 'bent' sources. Of this 'bent' class we estimate 75 per cent of sources to be intrinsically bent, as described in Section 3.3. Despite this, we include them as a class to demonstrate the usefulness of the method, which could be applied to BTs, S-shaped sources, and to explore transitions between lobed and tailed sources. Future work is planned to improve RL-XID to trace tailed emission more accurately and to filter out incorrect ridgelines to make this method more useful for selecting clean, science-ready source samples.

The remaining 3536 sources in the FRI-like morphology group not classified as 'bent' were classified as FRIs, 2354 of which are Q1 FRIs. Centre-brightened subgroups where the host galaxy was not in the central Gaussian distribution were classified as 'uncertain FRIs'; this class has 1295 sources.

If the subgroup contained sources with three SB peaks they were classified as 'triple-peaked' sources. There then remained a number of subgroups where the sources were either themselves one-sided or were one-sided due to the ridgeline tracing only part of the source. By one-sided, we mean that the source shows one bright peak and a tail of fainter emission. These sources were all placed into the 'one-sided ridgeline' class, which contains 2798 sources. From visually inspecting 100 random sources from this class, we estimate that ∼60 per cent are one-sided sources, the rest being incomplete or incorrect ridgelines. To test whether the more uncommon source classes (triple-peaked and one-sided ridgelines) could be preferentially affected by redshift selection effects, we compared their redshift distribution to the full sample and did not find them to be more prevalent at high redshift. In addition, we visually inspected the host IDs of 100 randomly chosen sources from these two classes and found only 5 per cent to be incorrect, consistent with the quality of the identifications for the full population (Hardcastle et al. 2023). Future work is planned to filter out incorrect ridgelines to make this class more useful for scientific investigation.

As our aim is to produce clean groups of sources with similar jet morphologies, through a method that considers the structural and physical properties of the jets, subgroups that were more heterogeneous (<85 per cent had the same morphology) were classified as 'other'. This class contains 5293 sources. A random selection of images from each class is shown in Fig. 5.

As an additional validation of our method, we compare our catalogue to Chilufya et al. (2025), who use visual inspection to classify 2893 RLAGN from LoTSS DR2 with spectroscopic classifications (Drake et al. 2024). Of the FRI and FRII sources in both this catalogue and Chilufya et al. (2025), 90 per cent of the classifications are consistent. Of the small proportion of sources that are not consistent, there is no clear class of objects that appears to be missing from this catalogue.

3.5 Selection biases

In this section, we consider the potential impact of selection effects on our conclusions. We emphasize that the aim of this work is to examine clean morphological samples, not to compare volume densities for different classes or compute luminosity functions. The complexity of the sample selection means that it is beyond the scope of this work to determine completeness corrections. We have carefully considered the potential impact of the biases summarised below on the science results presented in Section 4. The main biases in this sample are: (i) radio SB sensitivity; (ii) imposed angular size cut of 45 arcsec; and (iii) host galaxy selection as a function of redshift.

There are observational selection biases in classifying FRIs and FRIIs with 6 arcsec images. FRIIs are easier to resolve due to having two bright hotspots at a distance from the host galaxy. A higher SB sensitivity is needed to identify FRI jets fading out from the bright core (de Jong et al. 2024b; Ye et al. 2024). This can make it

Downloaded from https://academic.oup.com/mnras/article/541/4/3452/8161029 by Bibliotheek Instituut Moleculaire Plantkunde user on 30 January 2026

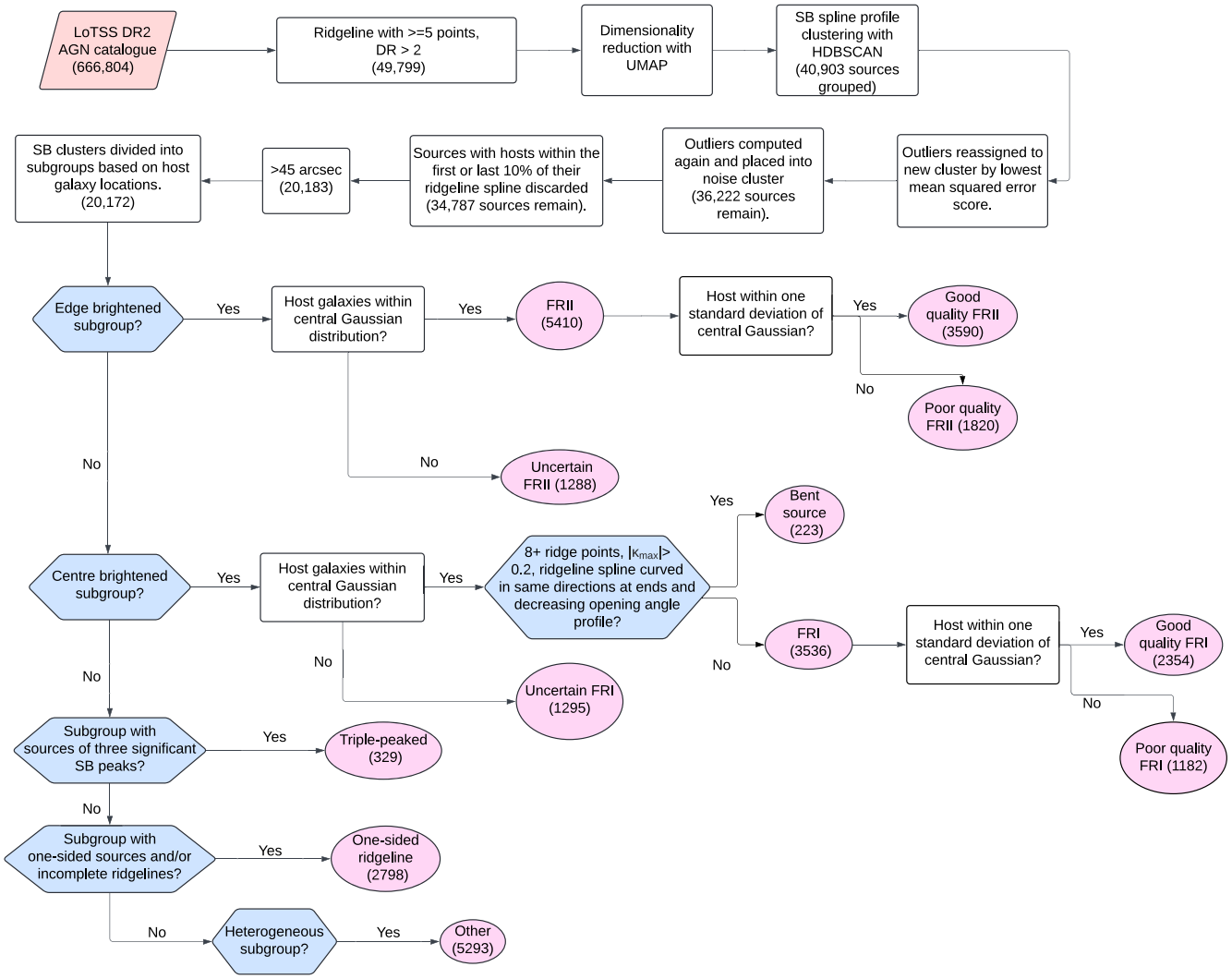

Figure 4. Flowchart outlining each stage in the classification process. Decisions about the final morphological labels are in hexagonal boxes and outputs are visible as circles.

Table 2. Final description of each class where Q1, Q2, and Q3 are quality flags corresponding to 1σ, 2σ, and 3σ intervals from the mean host location of each SB cluster GMM. Q1 sources are considered 'good quality' and are used for scientific analysis in Section 4. Q2 and Q3 sources are not used in our analysis due to having atypical host locations in comparison to the rest of their SB cluster.

Class	Description	Q1	Q2	Q3	Total
FRIs	In a centre-brightened SB cluster and host galaxy located within the central distribution of GMM	2354	1032	150	3536
'Bent' FRIs	FRI, $\geq$8 ridge points, $\lvert\kappa_{\max}\rvert > 0.2$, opposite κ direction at ridge ends, and decreasing $\theta_{\rm open}$ profile	143	80	0	223
Uncertain FRIs	In a centre-brightened SB cluster and host galaxy not within the central distribution of GMM	858	384	53	1295
FRIIs	In an edge-brightened SB cluster and host galaxy located within the central distribution of GMM	3590	1598	222	5410
Uncertain FRIIs	In an edge-brightened SB cluster and host galaxy not within the central distribution of GMM	786	481	21	1288
Triple peaked	Three significant SB peaks	218	102	9	329
One-sided ridgelines	One SB peak – contains one-sided sources and ridgelines	1788	942	68	2798
Other	Heterogeneous subgroups	3491	1622	180	5293

difficult to detect fainter FRIs at high redshift and often leads to an underestimation of their physical size. For this reason, and because we cannot account for projection angles, we refer to physical size as observed size. We do not expect the underestimation of FRI sizes to impact our classifications. Changes in source size would alter how the surface profiles are scaled, but the SB of the source would still decrease roughly monotonically with distance along the ridgeline. We tested the robustness of classifying faint FRIs by artificially lowering the sensitivity limit, step-by-step, until ∼97 per cent of the SB profiles fell below the sensitivity limit of the LoTSS images. We found that, unsurprisingly, as sources are scaled to lower SB, the outer parts of FRI plumes drop below the detection limit, changing the LAS and dynamic range of the source. Instead of these being allocated to an incorrect class, 80 per cent of these FRIs would be

Downloaded from https://academic.oup.com/mnras/article/541/4/3452/8161029 by Bibliotheek Instituut Moleculaire Plantkunde user on 30 January 2026

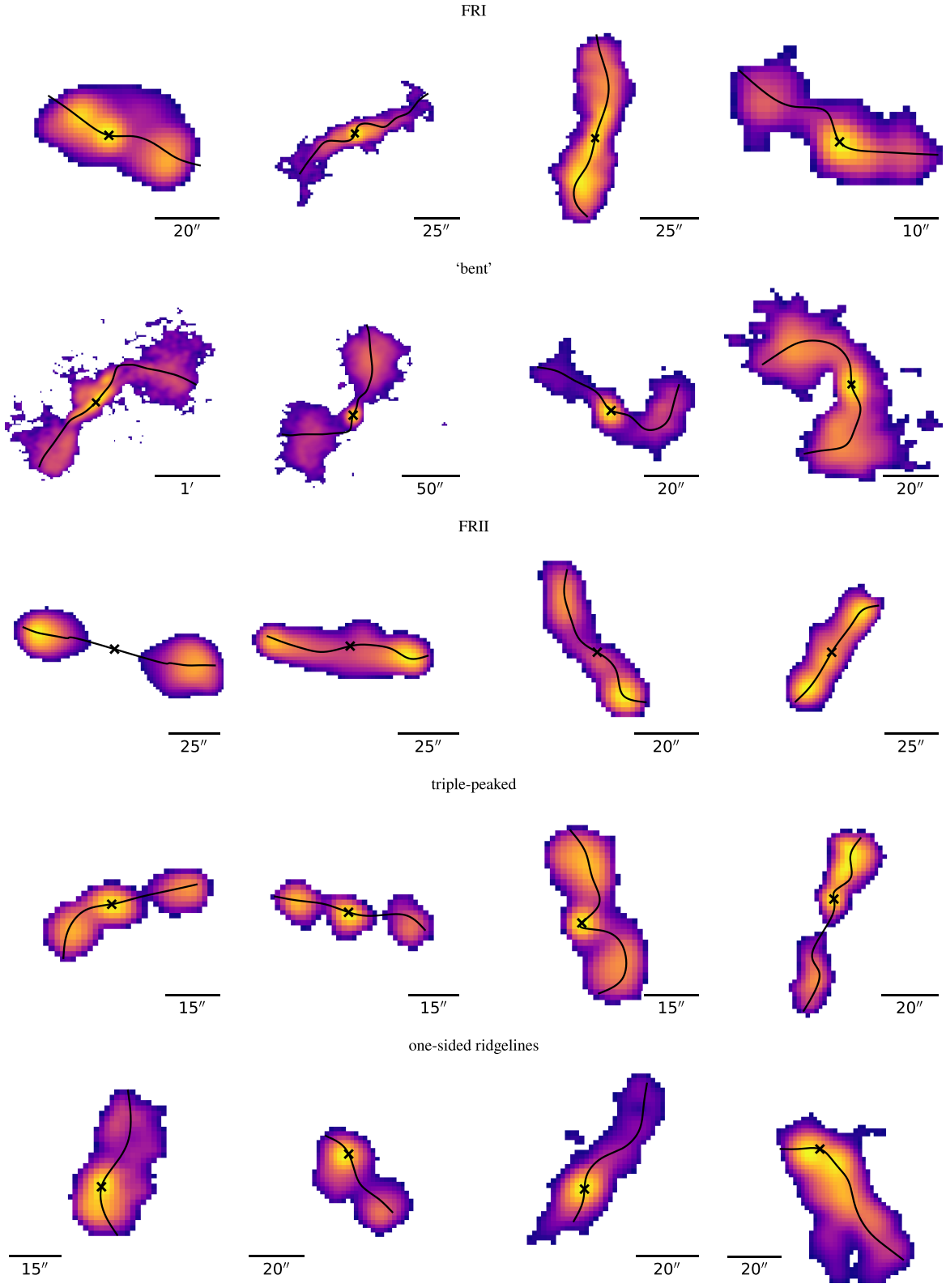

Figure 5. Randomly selected examples of sources in each morphological class. The solid lines in each figure correspond to that source’s ridgeline spline, and the crosses show the closest point on the ridgeline spline to the host galaxy. Each row corresponds to a different class, starting with FRIs, then FRIIs, bent, triple, and lastly one-sided ridgelines.

Downloaded from https://academic.oup.com/mnras/article/541/4/3452/8161029 by Bibliotheek Instituut Moleculaire Plantkunde user on 30 January 2026

excluded by the selection criteria (angular size and dynamic range thresholds). Where sources were not excluded, they were reassigned to a different FRI-like cluster, with a single-peak mean profile. de Jong et al. (2024a) found similar results in simulating how FRI and FRII morphological classifications change when the same source is observed at different redshifts, altering the observed SB. They found that only 2 per cent of FRIs presented as FRIIs. We note that in addition, the results we present in later sections do not depend on physical source size.

To resolve the smallest FRIs (below <45 arcsec), a balance would need to be found between angular resolution and SB sensitivity (de Jong et al. 2024b; Ye et al. 2024). We imposed a >45 arcsec cut in order to retain as many sources with well-sampled ridgelines for morphological analysis and distinguishable features in their SB profiles for HDBSCAN to identify as possible. We highlight here that this sample is likely missing a proportion of small FRIs. Very long baseline interferometry with LOFAR at various angular resolutions (0.3, 1, and 1.2 arcsec) would be the best way to ensure a more complete sample.

The redshift distributions of H25 are shown in their fig. 7. There is a steep decline in AGN listed in H25 above $z \sim 1.2$ as massive galaxies are no longer detected by the Legacy survey above this redshift. Host galaxy identifications become increasingly difficult at high redshift. High luminosity sources above $z > 1.5$ have been found to have a higher prevalence of bent morphologies and are less likely to be linear FRIIs (Miley & De Breuck 2008). However, we do not attempt to draw conclusions about the relative prevalence of different morphologies for any redshift ranges in this work.

Fig. 6 (bottom) shows the redshift distribution of sources classified as Q1 FRIs and FRIIs by our method. The two distributions are inherently different. The FRI sources are most commonly found at lower redshifts than the FRIIs. Above $z \geq 0.8$, the proportion of FRIIs begins to greatly exceed the proportion of FRIs. For these reasons, we will restrict our analysis to sources with $z \leq 0.8$ as described in Section 4. We consider the impact of selection effects introduced by the different redshift distributions of our morphological classes on our conclusions in later sections.

4 RESULTS

In this section, we report the radio properties of the Q1 (good quality) populations found from our classification method in Section 4.1 before investigating their host-galaxy properties in Section 4.2.

4.1 FRI and FRII radio properties

Fig. 6 shows that there is a large amount of overlap between size and luminosity distributions for the FRI and FRII populations. Substantial overlaps between the luminosity distributions of FRIs and FRIIs have only been observed in recent years (Best 2009; Gendre et al. 2010, 2013; Capetti et al. 2017; Mingo et al. 2019, 2022; de Jong et al. 2024a). Until then, it was thought that nearly all high-luminosity sources were FRIIs and low-luminosity sources were FRIs. The traditional luminosity break is around $L_{144} \sim 10^{26}$ WHz^{-1} (Fanaroff & Riley 1974). In our sample the median 144 MHz luminosities are 2.8×10^{25} WHz^{-1} and 2.6×10^{26} WHz^{-1} for the FRIs and FRIIs, respectively, and the median observed sizes are 384 and 463 kpc, respectively. Limiting our sample to $z \leq 0.8$, the median 144 WHz^{-1} luminosities become 1.8×10^{25} WHz^{-1} and 7.9×10^{25} WHz^{-1}, respectively, while the median observed sizes become 350 and 413 kpc.

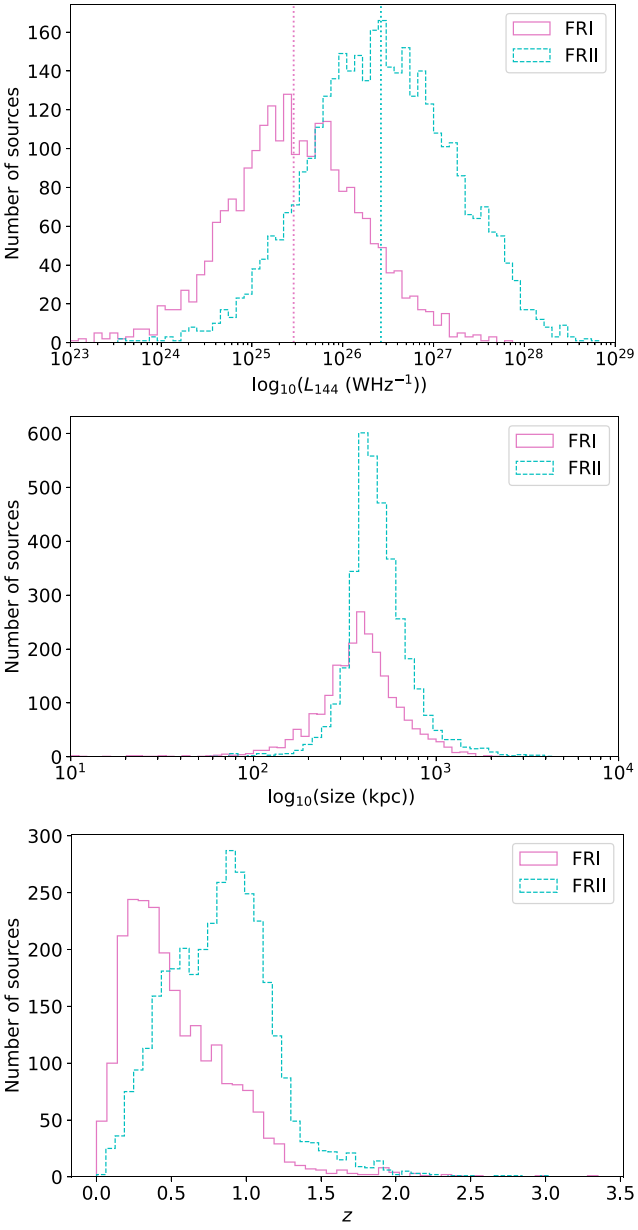

Figure 6. Radio luminosity at 144 WHz^{-1} (top), observed physical size in kpc (middle), and redshift (bottom) distributions for the Q1 FRI and FRII morphologies across the full redshift range of this sample. The vertical dotted lines in the top plot represent the median 144 WHz^{-1} luminosities of the two classifications.

For the full redshift range of our sample, almost a third (1089 or 30.3 per cent) of the sources in this sample classified as FRIIs have $L_{144} < 10^{26}$ WHz^{-1}, with 128 (3.6 per cent) having $L_{144} < 10^{25}$ WHz^{-1}. When limiting to $z \leq 0.8$, the proportion of low-luminosity FRIIs increases to 56.7 per cent. We will refer to FRIIs with $L_{144} < 10^{26}$ WHz^{-1} as 'FRII-lows'.

There also exists a number of Q1 FRIs that lie above the traditional luminosity break – 23.3 per cent of FRIs for the full redshift distribution and 9.7 per cent for $z \leq 0.8$. A small number of luminous FRIs are known to exist in the 3CRR and Mingo et al. (2019, 2022) catalogues. We will refer to FRIs with $L_{144} > 10^{26}$ WHz^{-1} as 'FRI-highs'.

Downloaded from https://academic.oup.com/mnras/article/541/4/3452/8161029 by Bibliotheek Instituut Moleculaire Plantkunde user on 30 January 2026

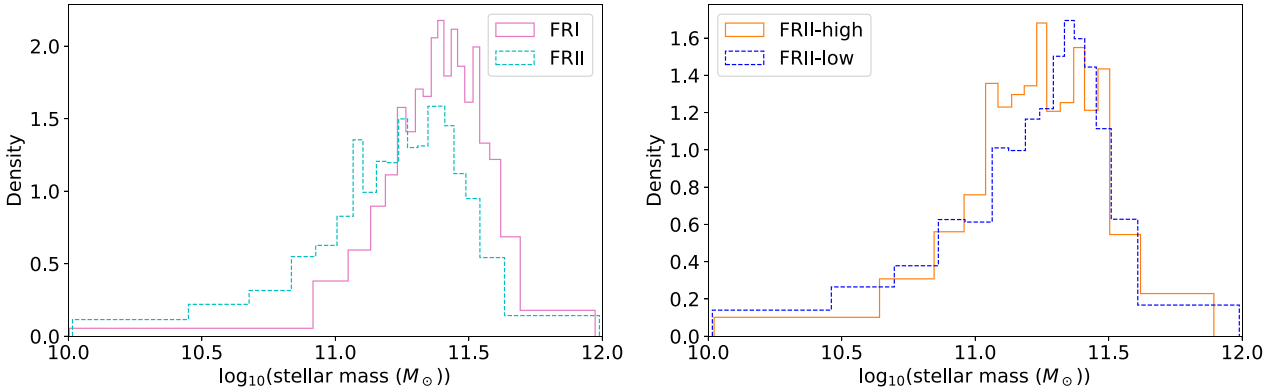

Figure 7. Left: Normalised distribution of host galaxy mass in $M_\odot$ for FRIs and FRIIs with $z \leq 0.8$. Right: The same distribution for FRII-highs and FRII-lows.

We now compare the FRI and FRII radio properties of this sample to other catalogues, in particular Mingo et al. (2019), where the authors use a semi-automated method to classify 5805 RLAGN from LoTSS Data Release 1. It is important to note that the ratios of FRIs to FRIIs in this work (3:5) differ significantly from that of Mingo et al. (2019), where the ratio is 3:1. For this method, which is based on automatically identifying features in SB profiles deduced by RL-XID, it is understandable that a higher proportion of FRIIs is identified, given their two distinct hotspots. It is also likely that many of our uncertain or more contaminated classes (e.g. one-sided ridgelines) contain sources that Mingo et al. (2019) would have classified as FRIs. We emphasize that it was not the aim of this work, nor that of Mingo et al. (2019), to estimate volume densities of FRIs or FRIIs, and both morphological samples are incomplete in different ways.

When considering Q1 sources at $z \leq 0.8$, the two populations have similar proportions of FRII-lows and FRI-highs. The FRI median luminosity of our sample is very similar to the values found by Mingo et al. (2019) and de Jong et al. (2024a), despite differences in the relative numbers of sources, method, and selection criteria. The median FRII luminosity of our sample is between the values found by Mingo et al. (2019) and de Jong et al. (2024a). We also reproduce some of the same conclusions as Mingo et al. (2019) in Section 4.

4.2 Host galaxy properties

4.2.1 Radio morphology and stellar mass

Radio morphology cannot be determined by jet power alone, demonstrated by the existence of large numbers of FRII-lows in this work and that of Mingo et al. (2019, 2022). A fundamental question is then whether differences in radio morphology are instead driven by properties of the host galaxy, large-scale environment, or a combination of factors.

In this section, we examine the relationship between radio morphology and stellar mass. We take stellar mass estimates from LoTSS DR2 (Hardcastle et al. 2023), which were calculated by adopting the approach of Duncan (2022). Briefly, stellar masses were estimated using spectral energy distribution modelling with code previously used by Duncan et al. (2014, 2019, 2021). These calculations were subject to certain assumptions about star formation history, metallicity, effects of nebular emission, and dust attenuation and are described by Hardcastle et al. (2023). The completeness of the stellar mass measurements is shown in fig. 14 of Hardcastle et al. (2023).

Fig. 7 shows the distribution of host galaxy masses for sources classified as FRIs and FRIIs (left) and FRII-highs and FRII-lows (right) by this work. The majority of sources in this sample have host galaxy masses $10.5 \leq \log_{10}(M/\mathrm{M}_\odot) \leq 12$, consistent with the completeness of stellar mass estimates by Hardcastle et al. (2023). While there is significant overlap between the host galaxy mass distributions of FRIs and FRIIs, differences can be seen in the most and least massive host galaxies. Massive galaxies (>11.5) are more likely to host an FRI, whilst the lower mass galaxies (<11.25) are more likely to have FRII morphology. There is a tail in the distribution of FRII-lows at low host galaxy mass, similar to that of Mingo et al. (2019). Including Q2 sources in this analysis does not significantly change the overall shapes of these distributions.

In order to ensure that this result is not caused by the different redshift distributions for FRIs and FRIIs noted in Section 3.5, in Fig. 8, we show the results of selecting a subsample of FRII-lows and FRIs near the FR luminosity break with $10^{25} \leq L_{144} \leq 10^{26}$ WHz^{-1} and 200 < observed size < 1000 kpc for $z \leq 0.8$ (top) and three different redshift bins (bottom) in our sample. The relationship between host stellar mass and radio morphology then becomes very clear. For intermediate radio luminosities, we find the likelihood of an RLAGN exhibiting FRI or FRII morphology is dependent on host galaxy mass. For masses greater than ∼11.25, the probability of forming an FRI becomes greater than the probability of forming an FRII-low. To test whether the stellar mass distributions for the two source populations are significantly different, we performed both a two-sample Anderson–Darling test (Scholz & Stephens 1987) (which is more sensitive to the tails of the distribution) and a Kolmogorov–Smirnov test (Massey 1951). For all redshift bins and for the unbinned sample, we found that the null hypothesis – that FRI and FRII-low subsamples are drawn from the same population – can be rejected at the >99 per cent level in both tests. In our sample, the correlation between FR class and host galaxy stellar mass is highly unlikely to be a redshift selection effect. Including Q2 sources in this analysis does not change this result.

We do not believe that the observed differences in stellar mass at the FR luminosity boundary can be attributed to environmental boosting of radio luminosity. Hardcastle (2018) found that the impact of environment on radio luminosity for jets of the same power is only a factor of 2–3 over a typical range of environments. In addition, the particle content of the FRIs and FRII-lows may be different (see e.g. Croston et al. 2018). Differences in particle content would decrease the radio luminosity of FRIs for a given jet power compared to FRIIs. We examined the group and cluster environments of the sources in our sample in the luminosity range near the FR break used for the

Downloaded from https://academic.oup.com/mnras/article/541/4/3452/8161029 by Bibliotheek Instituut Moleculaire Plantkunde user on 30 January 2026

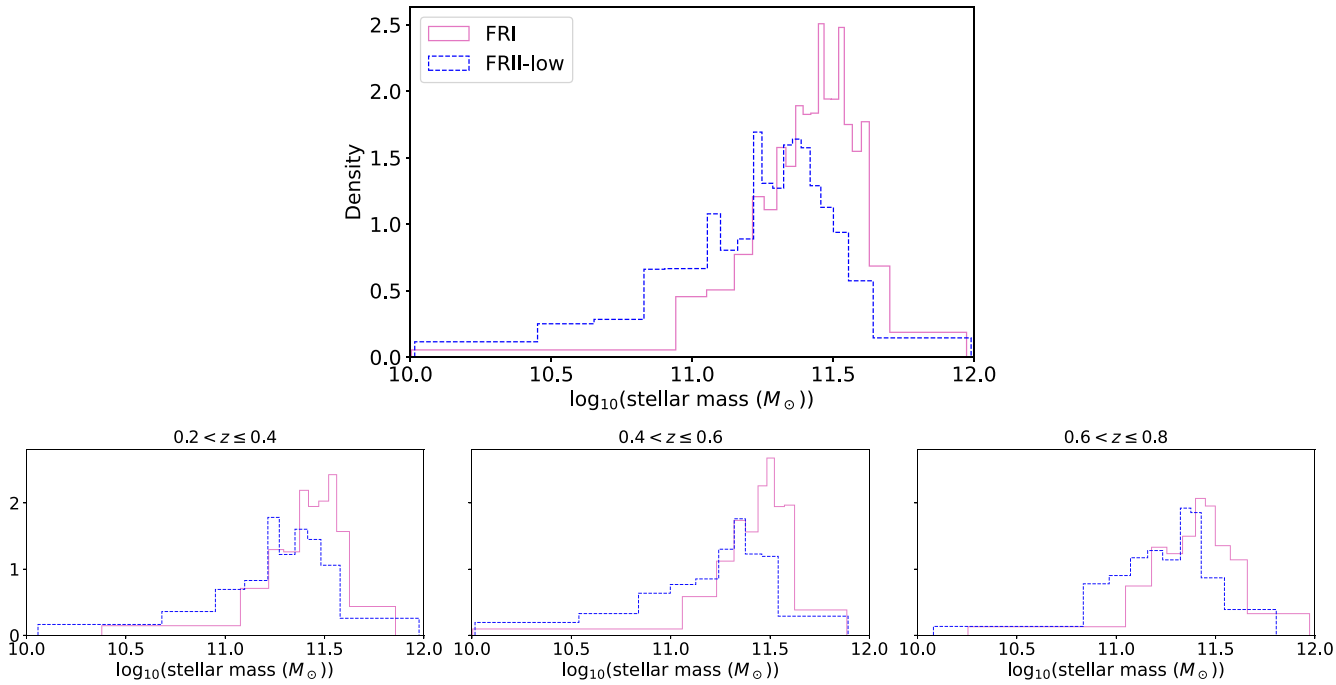

Figure 8. Top: Normalised histogram comparing the stellar mass distribution of FRIs and FRII-lows with $10^{25} \leq L_{144} \leq 10^{26}$ WHz^{-1} and 200 < size < 1000 kpc and $z \leq 0.8$. Bottom: The same plot for three different redshift bins.

analysis presented in Fig. 8, using the LoTSS DR2 environmental richness catalogue of Croston et al. (2025, MNRAS submitted). We find no evidence for a difference in the environmental distributions of the Q1 FRI and FRII-lows in the FR break luminosity range, with a Kolmogorov–Smirnov test (Massey 1951) showing that the null hypothesis that the two subsamples have the same parent population cannot be ruled out at 95 per cent confidence level. We, therefore, conclude that environmental differences between the FRIs and FRII-lows are unlikely to be causing a mismatch in the jet powers being compared.

However, there are a number of FRII-lows in high-mass galaxies, as there were in the sample of Mingo et al. (2022). This supports the theory that FRII-lows are likely to be a heterogeneous population. RLAGN are known to go through phases of activity (or duty cycles). Lobe morphology is typically determined on time-scales of the order of tens to hundreds of Myrs (see e.g. Konar et al. 2012, fig. 14 of Hardcastle 2018; Nandi et al. 2019). Some FRII-lows in high-mass galaxies could be fading FRII-highs that are no longer active, or whose jets have significantly powered down. Another consideration is the gas density and pressure in the inner kpc region of the host galaxy. If these are low, it could allow a low-power FRII to remain collimated.

4.2.2 *Exploring FR break dependence*

Ledlow & Owen (1996) were the first to suggest that the FR luminosity break was dependent on host galaxy absolute magnitude, used as a proxy for stellar mass (see e.g. Konishi et al. 2011). We now test this theory using the LoTSS DR2 stellar mass estimates. For the Q1 FRIs and FRIIs at $z \leq 0.8$ in our sample (see Fig. 9, top), we observe a slight increase in the FR break luminosity with stellar mass. To test whether this trend could be caused by selection effects, we examined it for three different redshift bins and performed a partial correlation test (see Fig. 9, bottom). We obtained $r = 0.2$ and $p = 0.5$, meaning that if redshift were a constant, no noticeable correlation would be found. Including Q2 sources in this analysis does not change this result. For this sample, we cannot rule out that selection effects are the cause of the observed trend between the FR break luminosity and stellar mass.

To eliminate the possibility that the observed lack of Ledlow–Owen relation in this sample is caused by systematic or selection effects in stellar mass estimates or by differences in the redshift distributions of the FRI and FRII subsamples (see Section 4.2.1 for a description of assumptions made when calculating stellar mass), we consider whether there is a relation between the FR break luminosity and host-galaxy (rest-frame) K-band magnitudes, K_s, taken from LoTSS DR2 (Shimwell et al. 2022; Hardcastle et al. 2023).

For all Q1 FRIs and FRIIs in this sample at $z \leq 0.8$, a noticeable increase in the FR break luminosity with increasing absolute magnitude is observed (see Fig. 10, top). This is statistically significant according to Spearman's rank correlation at >99 per cent confidence level. To determine if this relation was caused by selection effects, we examined it for three different redshift bins and performed a partial correlation test (see Fig. 10, bottom). We found that if redshift were constant, only a weak positive correlation ($r = 0.5$) between the FR break luminosity and K_s would remain at the 97 per cent significance level. For this sample, we cannot rule out that the observed dependence of the FR break luminosity on K_s is due to redshift selection effects. Including Q2 sources in this analysis does not change this result. We discuss our interpretations of this in Section 5.

4.2.3 *Specific star formation rate and radio morphology*

FRIs are thought to become mass loaded due to entrainment and disrupt on kpc scales (Bicknell 1994; Laing & Bridle 2002; Wykes et al. 2015; Hardcastle & Croston 2020). There are different ways that FRIs can entrain material, one of which is through

Downloaded from https://academic.oup.com/mnras/article/541/4/3452/8161029 by Bibliotheek Instituut Moleculaire Plantkunde user on 30 January 2026

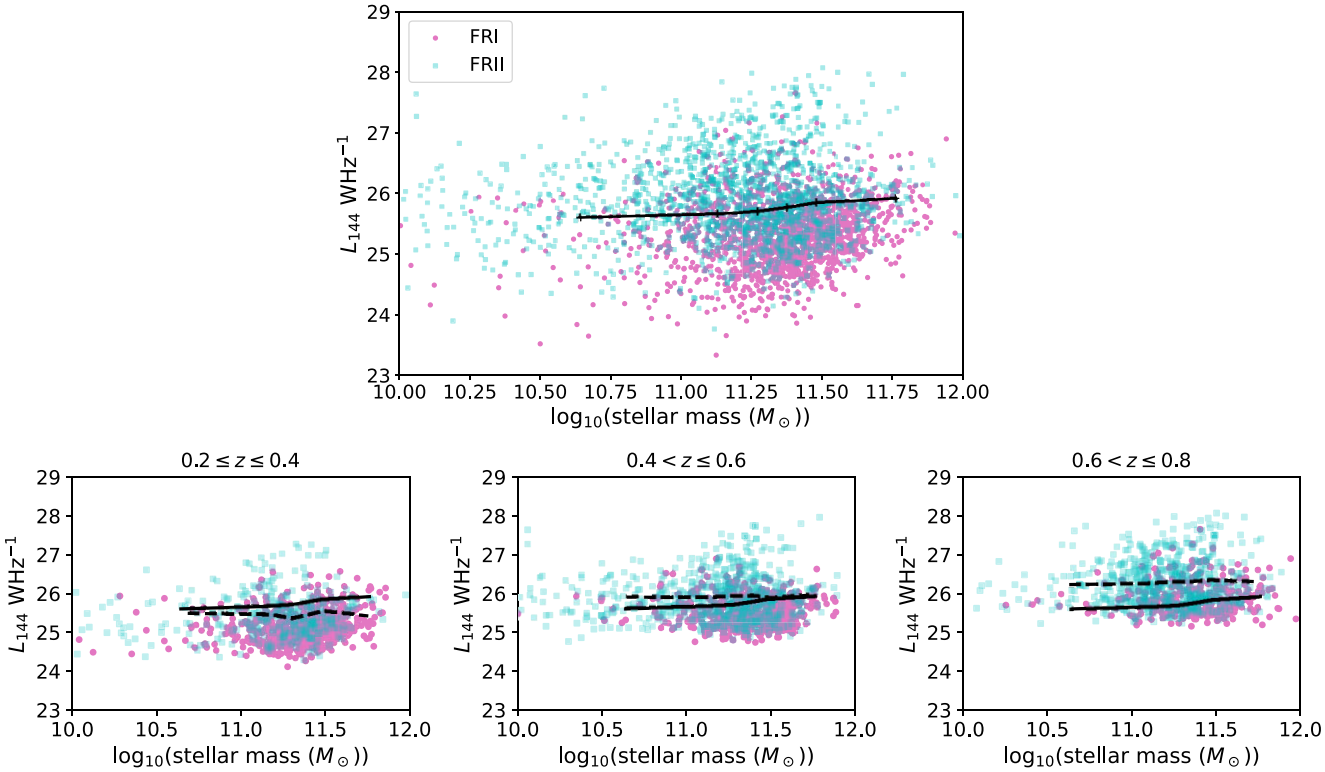

Figure 9. Top: The relationship between radio luminosity and stellar mass for the Q1 FRIs and FRIIs in this sample at $z \leq 0.8$. The solid line indicates the luminosity above which the normalised probability of finding an FRII exceeds that of finding an FRI in this sample. This is calculated across six equal-frequency bins in the range $10.25 \leq M \leq 12.0\,\mathrm{M}_\odot$. Bottom: The same plot for three different redshift bins, with dashed lines indicating the FR break luminosity for each redshift slice. The solid line shows the full sample relation as in the upper plot.

stellar winds from young stars. Therefore, the type of stellar population within the host galaxy could influence source evolution (see more in Section 1). We now investigate whether small-scale differences in host galaxy properties, such as the type of stellar population, influence radio morphology for sources of similar power.

We cross-matched the Q1 intermediate luminosity ($10^{25} \leq L_{144} \leq 10^{26}$) FRIs and FRII-lows in this sample, for $z \leq 0.8$, with the Max Planck Institute for Astrophysics and Johns Hopkins University (MPA–JHU) optical spectroscopic catalogue (Kauffmann et al. 2003; Brinchmann et al. ; Tremonti et al. 2004; Salim et al. 2007), based on data from the Sloan Digital Sky Survey Data Release 7 (SDSS DR7; Abazajian et al. 2009). It should be noted that this subsample is relatively small compared to our whole sample, consisting of 83 FRIs and 18 FRII-lows. For this subsample, we take the median specific star formation rate (sSFR) obtained from within the galaxy fibre aperture using nebular emission lines from MPA–JHU DR7 as described by Brinchmann et al. (). Fig. 11 shows the distribution of this subsample of FRIs and FRII-lows for different median sSFRs. It then becomes clear that in this subsample, the probability of producing an FRI exceeds the probability of producing an FRII-low in host galaxies with a higher median sSFR. To test whether the sSFR distributions for the two source populations are significantly different, we performed a two-sample Anderson–Darling test (Scholz & Stephens 1987). We found that the null hypothesis – that FRII-low and FRI samples are drawn from the same stellar population – can be rejected at the 97 per cent level.

5 DISCUSSION

In this paper, we have described a new automated method to classify RLAGN using ridgelines (Barkus et al. 2022) and its application to the LoTSS DR2 AGN catalogue (H25). This method has identified 2354 and 3590 Q1 FRIs and FRIIs, respectively. At each stage of the classification process, we visually inspected 100 randomly selected sources from each class and reported that ∼90 per cent of Q1 sources are correctly classified. We compared our FR classifications to those of Mingo et al. (2019) to check their quality. Restricting to $z \leq 0.8$, we find the proportion of FRII-lows and FRI-highs in our sample to be consistent with Mingo et al. (2019). In addition, the median 144 MHz luminosities of the FRIs and FRIIs are similar. We are confident that the Q1 FRI and FRII classes of sources can be used for science. We also identify 'bent', triple-peaked, and one-sided sources with this method. We believe that certain improvements to the ridgeline code are needed before using these categories for scientific analysis, as described in Section 3.4.

We first explored the physical properties of the FRI and FRII sources in this sample. We restricted our analysis to Q1 sources with $z \leq 0.8$ based on the redshift distributions of our catalogue and that of the parent sample H25. Although the FRIIs do have a higher median luminosity compared to the FRIs, we found a large amount of overlap between their luminosity distributions, supporting previous work that radio luminosity alone is not enough to classify morphology (as observed in other samples; Best 2009; Gendre et al. 2013; Mingo et al. 2019). The FRIIs also have a higher median size than the FRIs, but again, there is a large amount of overlap in the FRI and FRII size distributions. Furthermore, we find that 56.7 per cent

Downloaded from https://academic.oup.com/mnras/article/541/4/3452/8161029 by Bibliotheek Instituut Moleculaire Plantkunde user on 30 January 2026

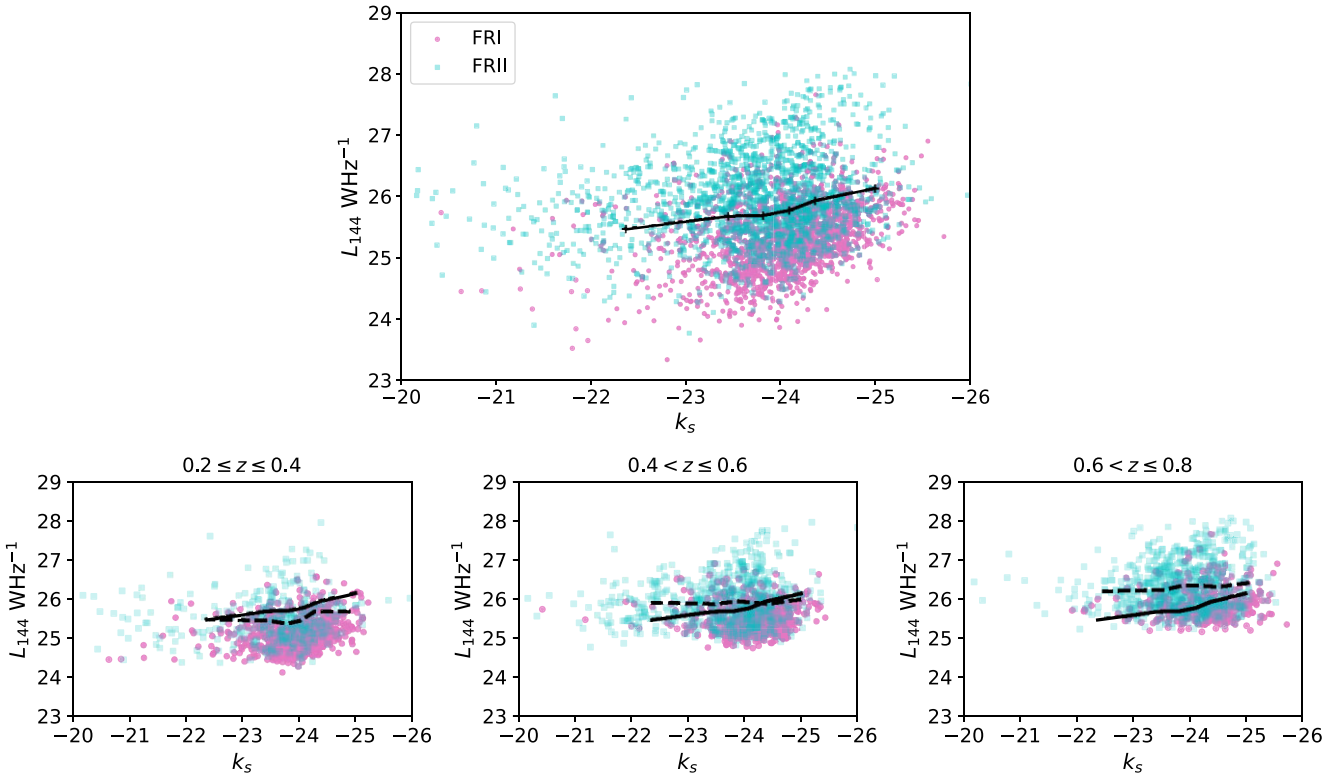

Figure 10. Top: The relationship between radio luminosity and host-galaxy rest-frame magnitude, K_s, for the Q1 FRIs and FRIIs in this sample at $z \leq 0.8$. The solid line indicates the luminosity above which the normalised probability of finding an FRII exceeds that of finding an FRI in this sample. This is calculated across six equal-frequency bins in the range $-25.5 \leq K_{\rm rest} \leq -21.5$. Bottom: The same plot for three different redshift bins, with dashed lines indicating the FR break luminosity for each redshift slice. The solid line shows the full sample relation as in the upper plot.

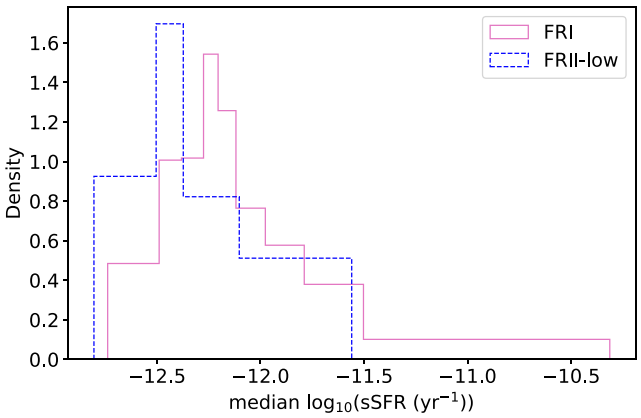

Figure 11. Normalised histograms comparing the median sSFR distributions, obtained from MPA–JHU DR7, of FRIs and FRII-lows with $10^{25} \leq L_{144} \leq 10^{26}$ WHz^{-1} and $z \leq 0.8$ in this sample.

of the FRIIs have $L_{144} < 1 \times 10^{26}$ WHz^{-1}. These results suggest that jet power alone is not enough to explain the FR dichotomy.

We instead considered whether morphological differences could be driven by properties of the host galaxy, large-scale environment, or a combination of factors. FRII jets are thought to remain relativistic throughout until terminating in a hotspot, while FRI jets are known to be initially relativistic and then become mass loaded due to entrainment, causing them to decelerate on kpc scales (Bicknell 1994; Laing & Bridle 2002; Wykes et al. 2015; Tchekhovskoy & Bromberg 2016; Hardcastle & Croston 2020). This suggests a relationship between jet power and environment. Ledlow & Owen (1996) found the FR break luminosity to be dependent on host-galaxy magnitude for the 3C sample (Mackay 1971). This result was initially thought to provide evidence to support a jet power–environment relationship as the cause of the FR divide. However, it has since been questioned due to severe selection effects (Hardcastle & Croston 2020).

We re-examined the Ledlow–Owen relation with our classified catalogue and found no evidence to support it when considering selection effects. We do not believe this disproves the idea that jets are disrupting due to environmental differences. The original relation was observed on a sample with severe selection biases. It was not known if it held across the full RLAGN population. Mingo et al. (2019) also could not rule out that the observed correlation between the FR break luminosity and host-galaxy absolute magnitude in their sample was due to selection effects. Furthermore, it is now known that the relationship between radio luminosity and jet power is subject to a lot of scatter due to external pressure, radiative losses, and differences in particle content of the two morphological types (Croston et al. 2018; Hardcastle & Croston 2020). This means that using radio luminosity as a proxy for jet power when exploring the jet disruption model may not be reliable.

Though the FR break luminosity may not be directly linked to host-galaxy stellar mass or absolute magnitude for this sample, we do find that for sources of similar size (200 $\leq$ size $\leq$ 1000 kpc) and luminosity near the FR break ($10^{25} \leq L_{144} \leq 10^{26}$ WHz^{-1}) the probability of forming an FRI exceeds that of forming an FRII-low in massive host galaxies, both for the full sample and for subsamples in three different redshift bins. The host galaxy stellar mass distributions for FRIs and FRII-lows are intrinsically different,

Downloaded from https://academic.oup.com/mnras/article/541/4/3452/8161029 by Bibliotheek Instituut Moleculaire Plantkunde user on 30 January 2026

and this is demonstrated with both a two-sample Anderson–Darling and Kolmogorov–Smirnov test at >99 per cent confidence. This result suggests that the inner environment is likely to have a role in determining when jets of a similar power disrupt, consistent with the conclusions of Bicknell (1994) and Laing & Bridle (2002).

As stellar populations have been postulated to play a role in jet disruption (see Section 1), we also compared the sSFRs of the FRIs and FRII-lows, as presented in Fig. 11. We find that the median sSFR of FRIs in this subsample is $1.7^{+0.4}_{-0.3}$ times larger than that of the FRII-lows. Though this result is tentative, we consider here the potential physical implications of our results on the ISM versus stellar wind entrainment models. First, we consider the results of Wykes et al. (2015), the only example of internal entrainment modelling on observational data. In Centaurus A, mass loading by stellar winds is sufficient to cause deceleration, but by a slim margin. The star formation rates (SFRs) we find in this work are a factor of 10 smaller than that of Centaurus A, so if stellar winds are only just sufficient to cause deceleration in Centaurus A, it is unlikely that this alone is enough to cause deceleration in all of our sources. In addition, we are considering more powerful FRIs near the FR break, for which Perucho et al. (2014) found mass loading by stellar winds to be insufficient. We, therefore, find it unlikely that mass loading from stellar winds is the cause of jet disruption in this sample.

An alternative scenario in which stellar activity could influence jet disruption was presented by Perucho (2020), who showed that the entry and exit of stars from jets can plausibly create a jet–ISM mixing layer. Basic consideration of a steady-state star formation scenario indicates that the observed sSFR difference between the FRIs and FRII-lows around the FR break luminosity would correspond to a small difference in the proportion of massive stars most relevant for this scenario. More detailed modelling work would be required to determine whether the relatively small difference in typical SFRs we observe for FRIs and FRII-lows around the FR break could be sufficient to influence the probability of jet disruption.

6 CONCLUSIONS

In this work, we have described a new automated method of classifying RLAGN using ridgelines (Barkus et al. 2022) and examined the physical and host-galaxy properties of the FRI and FRII jets identified by it. Our sample is based on data from the LoTSS DR2 AGN catalogue (H25) but also uses spectroscopic information from SDSS DR7 (Kauffmann et al. 2003; Brinchmann et al. ; Tremonti et al. 2004; Salim et al. 2007; Abazajian et al. 2009).

Our results have led to the following conclusions:

(i) Sources with FRI and FRII morphology can be found across a wide range of radio luminosities. On average, FRII sources do have a higher radio luminosity than FRIs, but there is a large amount of overlap.

(ii) When considering selection effects, we find no evidence that this sample supports the Ledlow–Owen relation in terms of stellar mass or host-galaxy rest-frame absolute magnitude.

(iii) For sources of intermediate observed size and luminosity near the FR break ($10^{25} \leq L_{144} \leq 10^{26}$ WHz^{-1}, 200 < observed size < 1000 kpc), the probability of forming an FRI or FRII is dependent on stellar mass. There are tentative indications that sSFR may also be relevant.

The cause of different morphologies in this RLAGN population is complex, but careful consideration of sources near the FR break ($10^{25} \leq L_{144} \leq 10^{26}$ WHz^{-1}) supports the role of inner environment in determining when jets of similar power disrupt. This catalogue is made publicly available and has the potential to enable further exploration into the impacts of jets on their environment. Future plans involve extending this classification method to include subclasses (e.g. lobed FRIs, tailed FRIs, and restarting sources) by improving the ridgeline drawing.

ACKNOWLEDGEMENTS

LC acknowledges support from the UK Research and Innovation (UKRI) Science and Technology Facilities Council (STFC) for a studentship (grant number ST/Y509449/1). JHC and BM gratefully acknowledge the support of UKRI STFC under grants ST/T000295/1 and ST/X001164/1. BM acknowledges support from UKRI STFC for an Ernest Rutherford Fellowship (grant number ST/Z510257/1). BB acknowledges support from STFC for a studentship under grant ST/X002543/1. MJH thanks STFC for support under grant ST/Y001249/1. JMGHJdJ recognizes support from project CORTEX (NWA.1160.18.316) of research programme NWA-ORC, which was (partly) financed by the Dutch Research Council (NWO). We thank Yifei Gong and Judith Ineson for useful discussions.

LOFAR is the LOw Frequency ARray designed and constructed by the Netherlands Institute for Radio Astronomy (ASTRON). It has observing, data processing, and data storage facilities in several countries, which are owned by various parties (each with their own funding sources), and which are collectively operated by the International LOFAR Telescope (ILT) foundation under a joint scientific policy. The ILT resources have benefited from the following recent major funding sources: INSU,CNRS, Observatoire de Paris, and Université d'Orléans, France; BMBF, MIWF-NRW, MPG, Germany; Science Foundation Ireland (SFI), Department of Business, Enterprise and Innovation (DBEI), Ireland; NWO, The Netherlands; the Science and Technology Facilities Council, UK; Ministry of Science and Higher Education, Poland; and the Istituto Nazionale di Astrofisica (INAF), Italy.

This research made use of the Dutch national e-infrastructure with support of the SURF Cooperative (e-infra 180169) and the LOFAR e-infra group. The Jülich LOFAR Long Term Archive and the German LOFAR network are both coordinated and operated by the Jülich Supercomputing Centre (JSC), and computing resources on the supercomputer JUWELS at JSC were provided by the Gauss Centre for Supercomputing e.V. (grant CHTB00) through the John von Neumann Institute for Computing (NIC).

This research made use of the University of Hertfordshire high-performance computing facility and the LOFAR-UK computing facility located at the University of Hertfordshire and supported by STFC under grant ST/P000096/1.

DATA AVAILABILITY

The RLAGN classified catalogue resulting from this work is available at https://lofar-surveys.org/dr2_release.html.

REFERENCES

Abazajian K. N. et al., 2009, ApJS, 182, 543
Barkus B. et al., 2022, MNRAS, 509, 1
Baron Perez N., Brüggen M., Kasieczka G., Lucie-Smith L., 2025, preprint (arXiv:2503.19111)
Begelman M. C., Blandford R. D., Rees M. J., 1984, Rev. Mod. Phys., 56, 255
Best P. N., 2009, Astron. Nachr., 330, 184

Downloaded from https://academic.oup.com/mnras/article/541/4/3452/8161029 by Bibliotheek Instituut Moleculaire Plantkunde user on 30 January 2026

Best P. N., Kauffmann G., Heckman T. M., Brinchmann J., Charlot S., Ivezić Ž., White S. D. M., 2005, MNRAS, 362, 25
Bicknell G. V., 1994, ApJ, 422, 542
Blanton E. L., 2000, PhD thesis, Columbia University, New York
Blanton E. L., 2015, Bending of WAT Radio Lobes in Abell 623 Through ICM Sloshing. Chandra proposal ID #17800069
Blanton E. L., Gregg M. D., Helfand D. J., Becker R. H., Leighly K. M., 2001, AJ, 121, 2915
Bowman M., Leahy J. P., Komissarov S. S., 1996, MNRAS, 279, 899
Bridle A. H., Perley R. A., 1984, ARA&A, 22, 319
Brinchmann J., et al., 2004, MNRAS, 351, 4, 1151
Burns J. O., Owen F. N., 1980, AJ, 85, 204
Campello, R.J.G.B. et al., 2013, Pacific-Asia Conference on Knowledge Discovery and Data Mining, 160
Capetti A., Massaro F., Baldi R. D., 2017, A&A, 601, A81
Chilufya J., Hardcastle M. J., Pierce J. C. S., Drake A. B., Baldi R. D., Röttgering H. J. A., Smith D. J. B., 2025, MNRAS, 539, 463
Croston J. H., Ineson J., Hardcastle M. J., 2018, MNRAS, 476, 1614
De Gazon G., Achong K.-M., Beltran Y., Morris M., Hooper E., Wilcots E., 2023, Am. Astron. Soc. Meeting Abstr., 55, 360.16
de Jong J. M. G. H. J. et al., 2024a, A&A, 683, A23
de Jong J. M. G. H. J. et al., 2024b, A&A, 689, A80
Drake A. B. et al., 2024, MNRAS, 534, 1107
Duncan K. J. et al., 2014, MNRAS, 444, 2960
Duncan K. J. et al., 2019, A&A, 622, A3
Duncan K. J. et al., 2021, A&A, 648, A4
Duncan K. J., 2022, MNRAS, 512, 3662
Edwards L. O. V., Fadda D., Frayer D. T., 2010, ApJ, 724, L143
Ekers R. D., 1978, A&A, 69, 253
Fanaroff B. L., Riley J. M., 1974, MNRAS, 167, 31P
Freeland E., Wilcots E., 2011, ApJ, 738, 145
Gendre M. A., Best P. N., Wall J. V., 2010, MNRAS, 404, 1719
Gendre M. A., Best P. N., Wall J. V., Ker L. M., 2013, MNRAS, 430, 3086
Golden-Marx E. et al., 2021, ApJ, 907, 65
Hardcastle M. J. et al., 2023, A&A, 678, A151
Hardcastle M. J. et al., 2025, MNRAS, 539, 1856(H25)
Hardcastle M. J., 2018, MNRAS, 475, 2768
Hardcastle M. J., Croston J. H., 2020, New Astron. Rev., 88, 101539
Hubbard A., Blackman E. G., 2006, MNRAS, 371, 1717
Jackson N., Rawlings S., 1997, MNRAS, 286, 241
Jones T. W., Owen F. N., 1979, ApJ, 234, 818
Kauffmann G. et al., 2003, MNRAS, 341, 33
Keenan M., Meyer E. T., Georganopoulos M., Reddy K., French O. J., 2021, MNRAS, 505, 4726
Kim D.-W., Fabbiano G., 2013, ApJ, 776, 116
Komissarov S. S., 1994, MNRAS, 269, 394
Konar C., Hardcastle M. J., Jamrozy M., Croston J. H., Nandi S., 2012, MNRAS, 424, 1061
Kondapally R. et al., 2022, MNRAS, 513, 3742
Konishi M. et al., 2011, PASJ, 63, S363
Laing R. A., Bridle A. H., 2002, MNRAS, 336, 1161
Ledlow M. J., Owen F. N., 1996, AJ, 112, 9
Lin Y.-T., Shen Y., Strauss M. A., Richards G. T., Lunnan R., 2010, ApJ, 723, 1119
Lukic V., Brüggen M., Mingo B., Croston J. H., Kasieczka G., Best P. N., 2019, MNRAS, 487, 1729
Mackay C. D., 1971, MNRAS, 154, 209
Massey F. J., 1951, J. Am. Stat. Assoc., 46, 68
McInnes L., et al. 2018, J. Open Source Softw., 3, 861
McInnes L., Healy J., Astels S., 2017, J. Open Source Softw., 2, 205
Meyer E. T., Fossati G., Georganopoulos M., Lister M. L., 2011, preprint (arXiv:1111.6490)
Miley G., 1980, ARA&A, 18, 165
Miley G., De Breuck C., 2008, A&AR, 15, 67
Mingo B. et al., 2019, MNRAS, 488, 2701
Mingo B. et al., 2022, MNRAS, 511, 3250
Morris M. E., Wilcots E., Hooper E., Heinz S., 2022, AJ, 163, 280
Morsony B. J., Miller J. J., Heinz S., Freeland E., Wilcots E., Brüggen M., Ruszkowski M., 2013, MNRAS, 431, 781
Mostert R. I. J. et al., 2021, A&A, 645, A89
Nandi S. et al., 2019, MNRAS, 486, 5158
O'Brien A. N., Norris R. P., Tothill N. F. H., Filipović M. D., 2018, MNRAS, 481, 5247
O'Dea C. P., Owen F. N., 1985, AJ, 90, 954
Owen F. N., Rudnick L., 1976a, ApJ, 203, 307
Owen F. N., Rudnick L., 1976b, ApJ, 205, L1
Perucho M., 2020, MNRAS, 494, L22
Perucho M., Martí J. M., Laing R. A., Hardee P. E., 2014, MNRAS, 441, 1488
Rudnick L., Owen F. N., 1976, ApJ, 203, L107
Salim S. et al., 2007, ApJS, 173, 267
Scholz F. W., Stephens M. A., 1987, J. Am. Stat. Assoc., 82, 918
Shimwell T. W. et al., 2022, A&A, 659, A1
Tasse C. et al., 2021, A&A, 648, A1
Tchekhovskoy A., Bromberg O., 2016, MNRAS, 461, L46
Tremonti C. A. et al., 2004, ApJ, 613, 898
Williams W. L. et al., 2019, A&A, 622, A2
Wing J. D., Blanton E. L., 2011, AJ, 141, 88
Wykes S., Hardcastle M. J., Karakas A. I., Vink J. S., 2015, MNRAS, 447, 1001
Ye H. et al., 2024, A&A, 691, A347

APPENDIX A: HOST SUBGROUPING

Sources with the same SB profiles but different host-galaxy positions do not belong in the same class, as the location of the host galaxy provides important information on the formation history and symmetry of the jets (the distance of each jet from the host galaxy). We examined the distributions of host-galaxy positions for each SB cluster and noticed that there were 1–3 peaks in the distributions. To separate the common host-galaxy locations within the SB clusters, we used GMM. Each Gaussian distribution that the GMM model identified was treated as a subgroup of its SB cluster, i.e. for each SB cluster, there were 1–3 subgroups of host positions, see Fig. A1 for examples of this.

Downloaded from https://academic.oup.com/mnras/article/541/4/3452/8161029 by Bibliotheek Instituut Moleculaire Plantkunde user on 30 January 2026

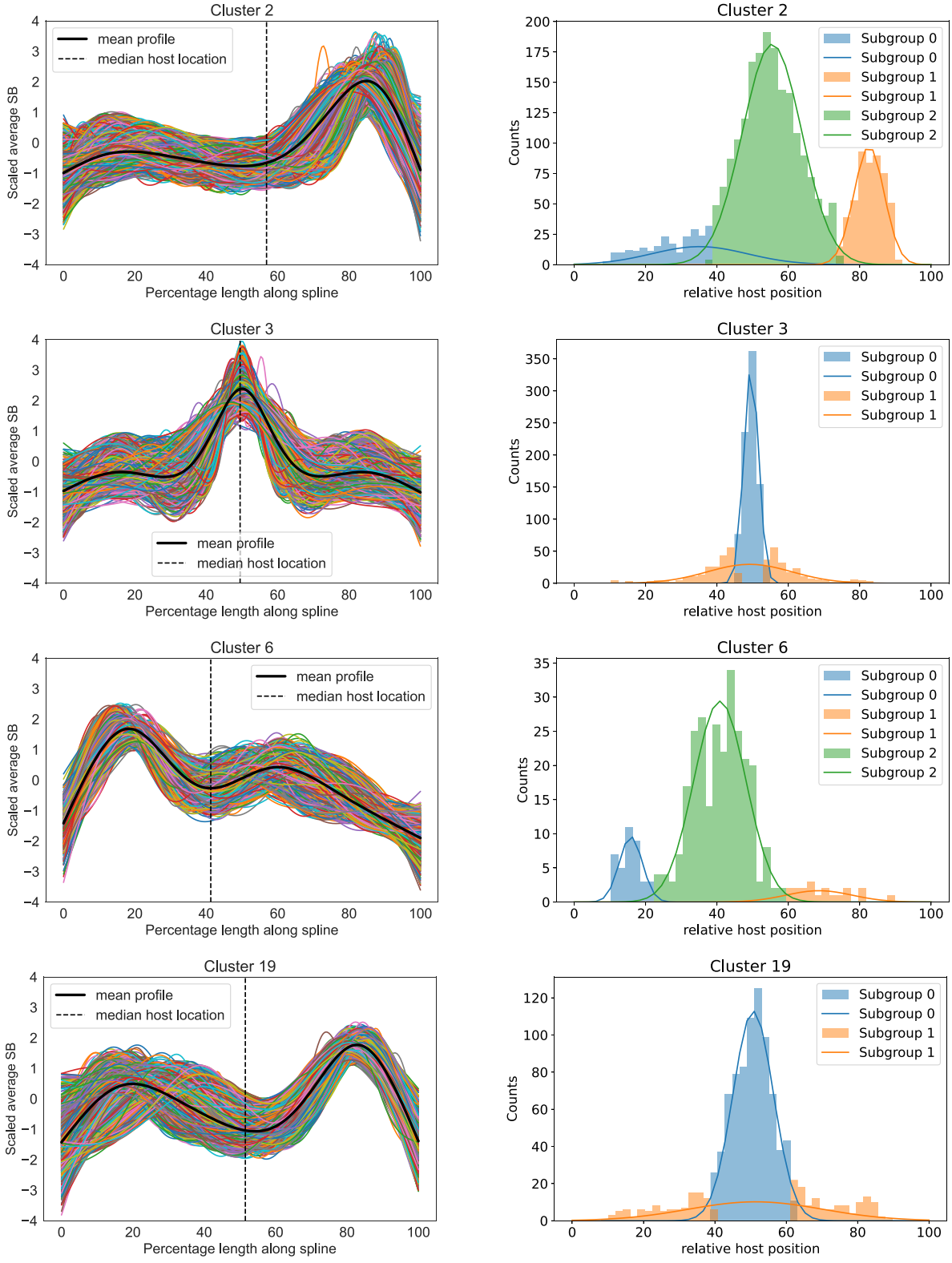

Figure A1. Left: SB clusters from HDBSCAN. Right: Corresponding host distributions, colour-coded by the subgroup number.

This paper has been typeset from a TEX/LATEX file prepared by the author.

© The Author(s) 2025.
Published by Oxford University Press on behalf of Royal Astronomical Society. This is an Open Access article distributed under the terms of the Creative Commons Attribution License (https://creativecommons.org/licenses/by/4.0/), which permits unrestricted reuse, distribution, and reproduction in any medium, provided the original work is properly cited.

Downloaded from https://academic.oup.com/mnras/article/541/4/3452/8161029 by Bibliotheek Instituut Moleculaire Plantkunde user on 30 January 2026